Shutdown dose rates in-cryostat outside the EU-DEMO vacuum vessel

T.A. Berry [a],[*], T. Eade [a], C. Bachmann [b], A. Čufar [c], T. Franke [b],[d], C. Gliss [b], D. Leichtle [e], C. Vorpahl [b]

[a] United Kingdom Atomic Energy Authority, CCFE, Culham Science Centre, Abingdon, Oxon, OX14 3DB, UK
[b] EUROfusion Consortium, Boltzmannstraße 2, Garching, D-85748, Germany
[c] Reactor Physics Department, Jožef Stefan Institute, Jamova cesta 39, Ljubljana, SI-1000, Slovenia
[d] Max Planck Institute for Plasma Physics, Boltzmannstraße 2, Garching, D-85748, Germany
[e] Karlsruhe Institute of Technology, Kaiserstraße 12, Karlsruhe, D-76131, Germany

ARTICLE INFO

ABSTRACT

Future fusion reactors using deuterium–tritium fuel will exhibit high fluences of high-energy neutrons inside and around the reactor vacuum vessel (VV). As well as causing material damage, fusion neutrons will activate materials, the decay of which leads to radiation fields in and around the reactor after shutdown. Gamma-ray emission from activated materials is a particular radiological hazard during periods of reactor shutdown. This must be accounted for in the design of the reactor shielding to ensure that risks are reduced as low as reasonably achievable.

Recent neutronics work has evaluated the shutdown dose rates (SDDRs) in the EU DEMOnstration power plant (DEMO) around the ports and throughout the cryostat, incorporating prospective shielding improvements to the VV and ports. Prior to the proposed shielding design improvements, calculations for the model including the helium-cooled pebble bed (HCPB) blanket showed that radiation leakage through the blanket and VV leads to biological-equivalent SDDRs (following 12 days' decay) above 10^3 μSv/h throughout the cryostat, ignoring additional contribution from radiation streaming through the port openings. Inclusion of the proposed VV changes reduces this dose rate to below 100 μSv/h. The work finds an approximate order-of-magnitude reduction in SDDR throughout the cryostat when all proposed shielding improvements are applied, leading to dose rates in the cryostat in the range of hundreds to thousands of μSv/h for the full model. The work shows that to further reduce dose rates inside the cryostat, improving the shielding performance of the ports is required, with particular emphasis on the lower port and the equatorial electron–cyclotron launcher which currently dominate the dose rates.

1. Introduction

Maintenance of a fusion reactor relies on dose rates in the maintenance areas being low enough for safe operations. High neutron fluxes in future fusion reactors including EU-DEMO will lead to neutron activation of materials inside the bioshield. The activated radionuclides will decay over time, producing a radiation field after shutdown which includes ionising and highly penetrative gamma rays. High shutdown dose rates (SDDRs) have safety implications for maintenance operations. This must therefore be accounted for in the reactor shielding design to ensure that risks are reduced as low as reasonably achievable.

Neutronics analysis of existing DEMO models has predicted dose rates exceeding 10^4 μSv/h in the cryostat (shown later in Fig. 6), while similarly high dose rates have also been predicted previously [1,2]. Lower SDDRs are preferred for maintenance operations, requiring improvements to the baseline shielding design. Leakage of fusion neutrons through the VV, plus leakage and streaming from the ports, are the major contributors to these ex-vessel SDDRs. Neutronics shielding performance improvements can be achieved by selecting materials with superior shielding properties, by removing direct streaming gaps in the case of port openings, and by adding shielding material. In this work several potential design changes are investigated for their effectiveness from a neutronics perspective.

1.1. Neutronics models

This analysis uses two DEMO neutronics models. Both are based on the 2017 DEMO baseline. A 22.5° sector model was used, exploiting symmetry effects with reflecting planes to reduce simulation effort. The breeding blanket (BB) modules consist of several homogenised radial
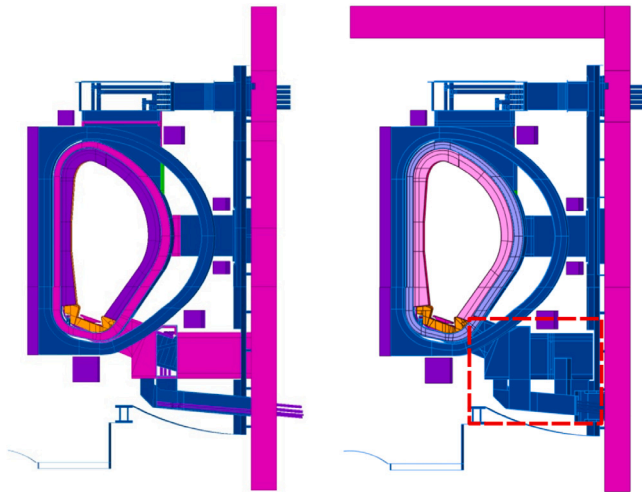

Fig. 1. DEMO 22.5° sector neutronics models used in present SDDR analysis (CAD shown) containing outboard midplane limiter. Left: previous (2019) model; right: updated (2020) model. Primary difference to base model is lower port design (marked by red box).

Fig. 2. Lower and upper inter-coil shield (ICS) locations in updated DEMO model, with lines representing locations of toroidal–poloidal slices shown on the right-hand side. Also labelled are poloidal coils (PC), toroidal coils (TC), vacuum vessel (VV), breeding blanket (BB) and divertor (DIV).

layers and the detailed divertor model contains homogenised layered plasma-facing components (PFCs). The previous (2019) model includes detailed ports, including the lower port pipe chase. The updated (2020) model uses an updated port geometry with increased detail in the lower port including pumps and port closure plates, and updates to the BB design.

Proposed improvements including inter-coil shields (ICS) and VV design changes were incorporated into the updated model. Further exploratory changes to the port shielding design were incorporated into the model individually to investigate their effect on SDDR. These are described further in the following sections. Both models are shown in Fig. 1.

For conservative results, the HCPB blanket implementation is used in analysis due to its weaker shielding properties compared to the water-cooled lithium-lead (WCLL) design.

1.2. Vacuum vessel shielding changes

Inter-coil shields are located at the upper and lower inboard of the VV, shown in Fig. 2, in order to reduce leakage to the cryostat. These consist of a Eurofer shell and Eurofer-plus-water (60:40 vol.%) bulk.

Proposed VV shielding changes are outlined in Fig. 3 and also described in [3]. The inner/outer stainless steel (SS) shell layers have been reduced in thickness from 60/60 to 32/42 mm on the inboard, and from 60/60 to 36/36 mm on the outboard. For the inboard VV, SS 316L(N)-IG in the shell and interspace structure (ribs) has been replaced with XM-19 for increased strength. The total approximate inboard VV thickness remains around 60 cm. An increase in the outboard thickness of 20 cm was seen as desirable in order to mitigate high in-cryostat dose rates due in part to leakage through the blanket and VV. To avoid design effort, for these exploratory calculations the change was approximated by an equivalent increase in the outboard material density. The final 10% of the radial thickness of the VV interspace was separated in the model geometry, and its density increased such that the quantity of 'additional material' is equivalent to a 20 cm thickness increase. This places the material as close as possible to the outside of the VV. The thickness increase close to the toroidal field coils (TFCs) was restricted in order to maintain a 10 cm separation, and the density change also varied depending on the cell thickness, which changes poloidally. For thin (6 cm plus an increase of 20 cm), thick (7.25 cm plus 20 cm) and restricted (5.4 cm plus 6 cm) outboard outer layer
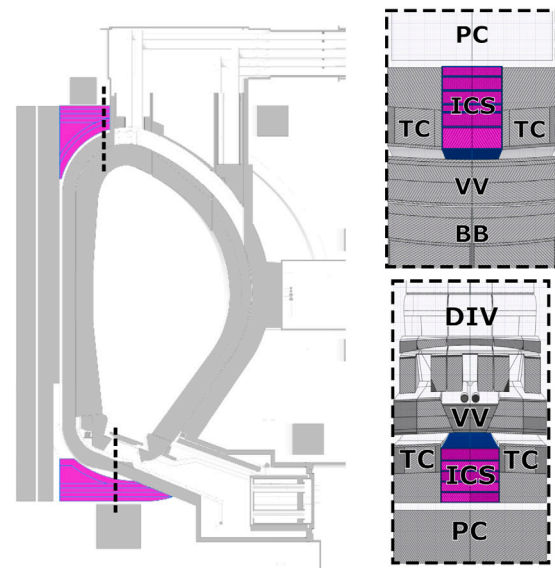

Fig. 3. Previous (top) and proposed (bottom) inboard and outboard VV designs including composition of shell (grey) and body or interspace (pink). Lower side is closest to plasma. Layer thicknesses are given in millimetres.

cells, the density was multiplied by factors of 4.33 (= 26/6), 3.76 (= 27.25/7.25) and 2.11 (= 11.4/5.4) respectively.

Finally, the material of the shielding plates of the VV interspace – comprising the majority of the SS material – was changed. For roughly the innermost 40% of the VV interspace (closest to the plasma) Eurofer plates are used (for waste reduction), while in the remainder of the layers boronated 304B4 (for neutron shielding) is used.

1.3. Port shielding changes

Port shielding improvements are evaluated individually. For the lower and upper ports, thickness increases to the walls are made using density increases. For the upper port a uniform 30 cm thickness increase is made to all walls, excluding those adjacent to the TFCs in order to maintain a 10 cm gap. For the lower port the increase varies from 10 cm, up to 20 cm for the upper wall where the leakage to the cryostat is severe.
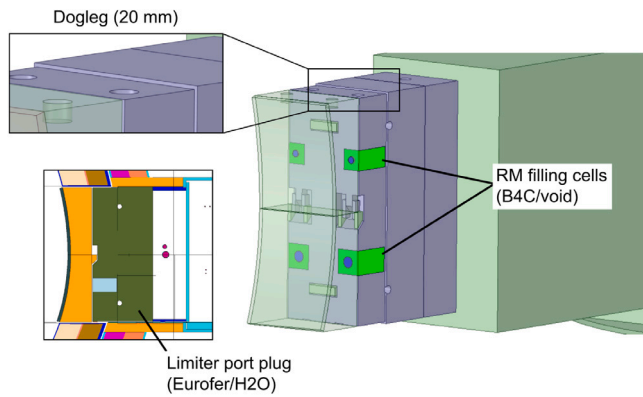
Fig. 4. Outboard midplane limiter model (CAD) labelling shielding improvements. Inset: MCNP radial–poloidal slice through limiter including port plug with 41 cm thickness increase applied.
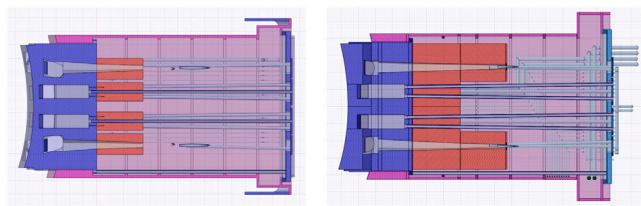

Fig. 5. Radial–poloidal slice through electron–cyclotron (EC) showing design changes. Left: previous model; right: updated model including larger waveguide shields.

For the equatorial port, two port configurations are evaluated: the outboard midplane limiter (not including lower limiter) and the electron–cyclotron launcher (EC). The basic design of the limiter is consistent between previous and new models. A dogleg junction in the limiter at the outer VV radius, of 20 mm, is added to reduce the streaming of neutrons down the 10 mm gaps around the limiter. An increase in thickness of the Eurofer-plus-water port plug (behind the front shielding block) is made to reduce leakage; increases of 20 cm and 41 cm were evaluated separately. Finally, slots in the limiter block which exist for remote maintenance were filled with boron carbide (B_4C) powder. These changes are shown in Fig. 4.

The EC design [4] includes updated larger waveguide shields internal to the EC, which shield the neutrons streaming down the waveguide openings. The design is also mirrored toroidally to achieve more realistic separation of the adjacent ports, an artefact of the reflecting planes in the neutronics model. These changes are shown in Fig. 5.

It should be noted that due to the reflecting planes used in the neutronics model, analysis of a model containing a given outboard equatorial port configuration produces results which assume that configuration in every port, when the final design will contain a variety of equatorial port configurations toroidally. Therefore limiter models produce optimistic SDDR results, while EC models lead to overly conservative results.

2. Methodology

The CCFE-developed MCR2S (Mesh-Coupled Rigorous 2-Step) [5] cell-under-voxel workflow [6] was used to generate photon sources for photon transport calculations in MCNP6.2. Neutron fluxes across the DEMO sector were calculated in MCNP 6.2 [7] using a cell-under-voxel mesh tally, which records cells, materials and densities underneath each mesh voxel. The mesh used a resolution of 20 cm covering the whole model, and the MCR2S cell rejection sampling capability further improves the resolution of the photon source. Cross-section data from JEFF-3.3 [8] were used and fluxes were recorded in 175 energy groups.

Table 1
DEMO phase 1 irradiation schedule used in the present analysis.

Duration	Fusion power (MW)	Repetition
5.173 yr	599.4	Once
1 h	0.0	48 times
4 h	1998	

Iteratively-generated weight window meshes, created with the CCFE MAGIC tool [9], were applied to the neutron transport calculations. Photon transport calculations did not use variance reduction, but uniform voxel sampling was used in order to sample photon emission throughout the model, reducing statistical error outside the VV.

MCR2S used EAF-2010 [10] nuclear data to perform automated FISPACT-II calculations [11] for each cell, material and density underlying each voxel, in order to generate 'common decay source' meshes for photon transport calculations. This was performed for the DEMO Phase 1 irradiation schedule (5.2 calendar years at 1998 MW, 20 displacements per atom (DPA) first-wall equivalent) shown in Table 1. The decay time was 12 days: this is a conservative time for maintenance but is known to give similar results to a 30-day decay time.

Photon transport calculations were performed in MCNP6.2 with the 12-day decay file as a source, using photon interaction cross-sections from MCPLIB84. Mesh tallies across individual ports and coarser tallies covering the whole model were recorded. These results were calculated applying ICRP-74 biological-equivalent dose rate multipliers [12] as used in the International Thermonuclear Experimental Reactor (ITER), giving results in terms of µSv/h.

In some of the calculations, ports are blocked in order to isolate sources of high dose rate. When a port is blocked, all neutrons and photons passing through the port opening are stopped and do not contribute to results.

SDDR calculations were performed on CCFE's high-performance computing clusters. The combined real time of the neutron transport, inventory and photon transport calculations was approximately 60 h on 128 cores, for a typical model.

3. Results

SDDRs throughout the model for a 12-day decay time are shown in Fig. 6, and results at selected locations inside and around the ports are given in Table 2. The combined shielding improvements result in approximate order-of-magnitude reductions in leakage in their respective locations. With all proposed changes in place (including an outboard midplane limiter port plug thickness increase of 20 cm), dose rates of hundreds of µSv/h are possible in the cryostat, rising to thousands of µSv/h close to the VV. Outside the VV and ports, the dose rate would only reach above 10^4 µSv/h around the edges of the lower port. It is also observed that the addition of inter-coil shields successfully mitigate the high cryostat dose rates previously calculated on the upper inboard and below the divertor (points A and G in Table 2).

By isolating ports (blocking all others), we can probe the effect of individual changes. In Fig. 7 the SDDR around the equatorial port is shown with proposed limiter shielding changes implemented, including a 20 cm shield block thickness increase.

The results show that dose rates below 10^3 µSv/h in the majority of the equatorial port are achievable with the improved limiter shielding, and that after the improvements, shielding at the corners of the port adjacent to the VV should be prioritised, as it is here that leakage dominates the SDDR in the cryostat.

The results in Fig. 8 show that for the lower and upper ports, wall thickness increases are effective in reducing dose rates in the cryostat around the ports. For the lower port, before the changes dose rates exceeding 10^4 µSv/h extended around much of the port and VV. The port wall thickness increase reduces dose rates to below 10^4 µSv/h
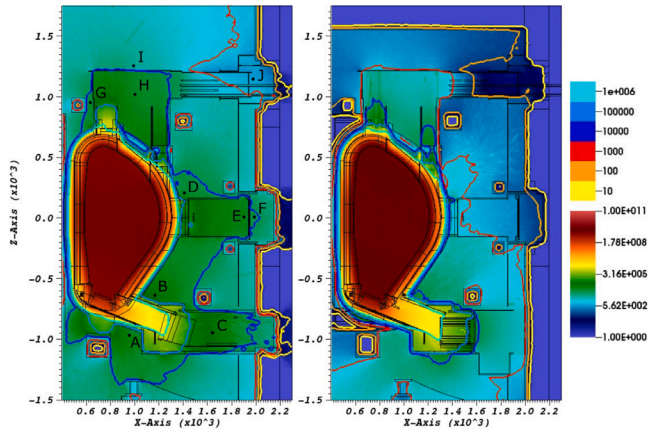
Fig. 6. Radial–poloidal slices showing 12-day biological-equivalent SDDR results for (left) previous model and (right) model containing all proposed shielding improvements and with equatorial port limiter. Dark blue, red, orange and yellow contours represent 10^4, 10^3, 100 and 10 μSv/h respectively. Labels A to J mark points in Table 2.

Fig. 7. Radial–poloidal slice showing 12-day biological-equivalent SDDR result around equatorial port, with lower and upper ports blocked and including shielding improvements to outboard midplane limiter. Dark blue, red, orange and yellow contours represent 10^4, 10^3, 100 and 10 μSv/h respectively.

Fig. 8. Radial–poloidal slices showing 12-day biological-equivalent SDDR results around lower and upper ports, with other ports blocked. Shown are lower port (a) before and (b) after port wall thickness increases, and upper port (c) before and (d) after port wall thickness increases. Dark blue, red, orange and yellow contours represent 10^4, 10^3, 100 and 10 μSv/h respectively.
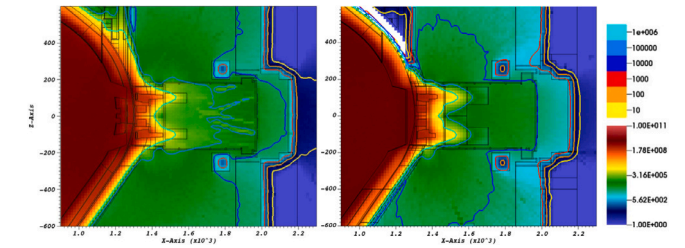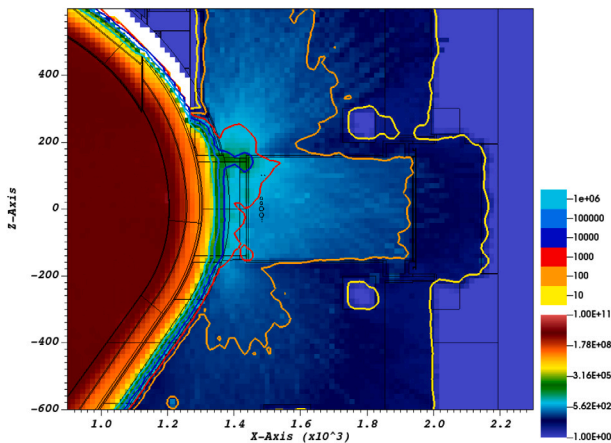

Fig. 9. Radial–poloidal slices showing 12-day biological-equivalent SDDR results around equatorial port EC, with lower and upper ports blocked. Left: previous model; right: updated model with reflected geometry and larger waveguide shields. Dark blue, red, orange and yellow contours represent 10^4, 10^3, 100 and 10 μSv/h respectively.

Table 2
SDDR results (12-day biological-equivalent) for previous (2019) model and model containing all proposed shielding improvements with equatorial port limiter. Results are taken at points labelled in Fig. 6. Δ is the change in SDDR between the previous model and the improved model, i.e. $\Delta = -81\%$ indicates that the biological-equivalent SDDR at point A is 81% lower in the improved model, compared to the previous model.

	Previous Result/μSv/h	Improved Result/μSv/h	Δ
A	1.90E+04 ± 5%	3.59E+03 ± 7%	−81%
B	4.61E+04 ± 3%	9.43E+03 ± 5%	−80%
C	4.63E+04 ± 1%	9.78E+03 ± 2%	−79%
D	2.27E+04 ± 3%	3.85E+03 ± 3%	−83%
E	1.81E+04 ± 4%	4.03E+02 ± 2%	−98%
F	1.33E+04 ± 7%	1.98E+02 ± 2%	−99%
G	1.45E+04 ± 1%	7.90E+02 ± 3%	−95%
H	1.62E+04 ± 1%	3.00E+03 ± 1%	−82%
I	3.65E+03 ± 1%	5.44E+02 ± 3%	−85%
J	6.36E+02 ± 1%	3.13E+01 ± 1%	−95%

everywhere aside from the top of the port. For the upper port, the port wall thickness increase reduces dose rates to below 10^3 μSv/h everywhere around the port, and to below 100 μSv/h closer to the bioshield (point J in Table 2).

Neutronics results for the EC designs have been discussed previously in Refs. [13,14]. In Fig. 9 the SDDR results are compared for the previous and updated EC designs. The larger waveguide shields in the updated model reduce the extent of the 10^4 μSv/h SDDR contour in the cryostat, and reduce the dose rate inside the equatorial port. By comparison with the limiter results in Fig. 7, it is clear that the EC port configuration leads to greater SDDRs in and around the port due to the waveguide penetrations. The shape of the contours indicates that improved shielding at the corners of the port would lead to a further reduction in cryostat dose rates.

It is also useful to note that towards the bottom of Fig. 7, the contours show that the blanket and VV shielding changes have the potential to reduce dose rates in the cryostat to below 100 μSv/h, when leakage from the ports is removed. From this work it is therefore found that were these changes to be implemented, further improvements in the blanket and VV shielding capability would not be a priority in reducing SDDRs as the ports now dominate.

4. Discussion and conclusions

It has been found in this analysis that the sum of the proposed changes to the HCPB blanket, VV and lower, equatorial and upper ports leads to an approximate order-of-magnitude reduction in SDDR throughout the cryostat. Proposed changes to the VV design lead to a similar reduction in neutron flux leakage. Each of the changes investigated is effective and so they can be recommended from a neutronics perspective, as they would be important in obtaining SDDRs as low as reasonably achievable.
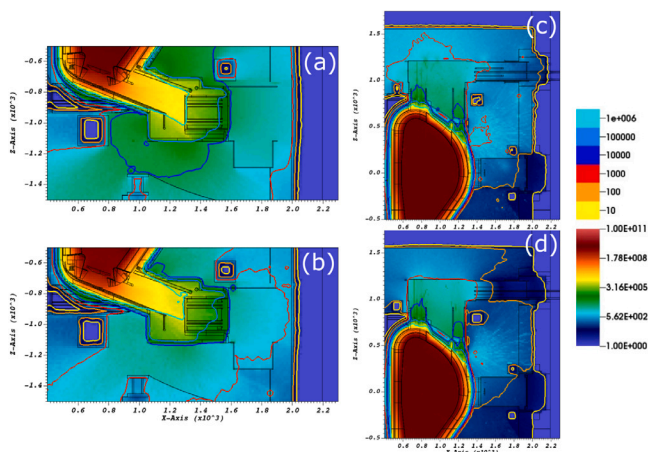
Following these changes, SDDRs inside the cryostat are dominated by leakage from the top of the lower port and by leakage from the corners of the equatorial port, both for the limiter and EC configurations. Further targeted shielding could therefore be beneficial in further reducing SDDRs, while further blanket and VV improvements are expected to have less impact.

The changes would be beneficial from a safety perspective, considering both the biological effects and the effect of high doses on equipment. The advantages would need to be balanced with engineering and remote maintenance requirements for DEMO. Further work could include evaluation of targeted shielding to address key sources of high dose rates. This could be combined with a more thorough evaluation of the dose rate limits in given areas with attention to operational and maintenance requirements, to ensure that modifications are effective.

Declaration of competing interest

The authors declare that they have no known competing financial interests or personal relationships that could have appeared to influence the work reported in this paper.

Data availability

Data will be made available on request.

Acknowledgements

References

[1] I. Palermo, R. Villari, A. Ibarra, Shutdown dose rate assessment with the Advanced D1S method for the European DCLL DEMO, Fusion Eng. Des. 122 (2017) 163–175, http://dx.doi.org/10.1016/J.FUSENGDES.2017.08.021.

[2] C. Bachmann, S. Ciattaglia, F. Cismondi, T. Eade, G. Federici, U. Fischer, T. Franke, C. Gliss, F. Hernandez, J. Keep, M. Loughlin, F. Maviglia, F. Moro, J. Morris, P. Pereslavtsev, N. Taylor, Z. Vizvary, R. Wenninger, Overview over DEMO design integration challenges and their impact on component design concepts, Fusion Eng. Des. 136 (2018) 87–95, http://dx.doi.org/10.1016/J.FUSENGDES.2017.12.040.

[3] C. Bachmann, L. Ciupinski, C. Gliss, T. Franke, T. Härtl, P. Marek, F. Maviglia, R. Mozzillo, R. Pielmeier, T. Schiller, P. Spaeh, T. Steinbacher, M. Stetka, T. Todd, C. Vorpahl, Containment structures and port configurations, Fusion Eng. Des. 174 (2022) 112966, http://dx.doi.org/10.1016/J.FUSENGDES.2021.112966.

[4] T. Franke, G. Aiello, K. Avramidis, C. Bachmann, B. Baiocchi, C. Baylard, A. Bruschi, D. Chauvin, A. Cufar, R. Chavan, C. Gliss, F. Fanale, L. Figini, G. Gantenbein, S. Garavaglia, G. Granucci, J. Jelonnek, G.S. López, A. Moro, M. Moscheni, N. Rispoli, M. Siccinio, P. Spaeh, D. Strauss, F. Subba, I. Tigelis, M.Q. Tran, C. Tsironis, C. Wu, H. Zohm, Integration concept of an electron cyclotron system in DEMO, Fusion Eng. Des. 168 (2021) http://dx.doi.org/10.1016/j.fusengdes.2021.112653.

[5] A. Davis, R. Pampin, Benchmarking the MCR2S system for high-resolution activation dose analysis in ITER, Fusion Eng. Des. 85 (1) (2010) 87–92, http://dx.doi.org/10.1016/J.FUSENGDES.2009.07.002.

[6] T. Eade, B. Colling, J. Naish, L.W. Packer, A. Valentine, Shutdown dose rate benchmarking using modern particle transport codes, Nucl. Fusion 60 (5) (2020) 056024, http://dx.doi.org/10.1088/1741-4326/ab8181.

[7] C.J. Werner, J.S. Bull, C.J.J. Solomon, F.B. Brown, G.W. Mckinney, M.E. Rising, D.A. Dixon, R.L. Martz, H.G.I. Hughes, L.J. Cox, A.J. Zukaitis, J.C. Armstrong, R.A. Forster III, L. Casswell, MCNP Version 6.2 Release Notes, Tech. Rep. LA-UR-18-2, Los Alamos National Laboratory, 2018.

[8] A.J.M. Plompen, O. Cabellos, C. De, M. Fleming, A. Algora, M. Angelone, P. Archier, E. Bauge, O. Bersillon, A. Blokhin, F. Cantargi, A. Chebboubi, C. Diez, H. Duarte, E. Dupont, J. Dyrda, B. Erasmus, L. Fiorito, U. Fischer, D. Flammini, D. Foligno, M.R. Gilbert, J.R. Granada, W. Haeck, F.-J. Hambsch, P. Helgesson, S. Hilaire, I. Hill, M. Hursin, R. Ichou, R. Jacqmin, B. Jansky, C. Jouanne, M.A. Kellett, D.H. Kim, H.I. Kim, I. Kodeli, A.J. Koning, A.Y. Konobeyev, S. Kopecky, B. Kos, A. Krása, L.C. Leal, N. Leclaire, P. Leconte, Y.O. Lee, H. Leeb, O. Litaize, M. Majerle, J.I. Márquez Damián, F. Michel-Sendis, R.W. Mills, B. Morillon, G. Noguère, M. Pecchia, S. Pelloni, P. Pereslavtsev, R.J. Perry, D. Rochman, A. Röhrmoser, P. Romain, P. Romojaro, D. Roubtsov, P. Sauvan, P. Schillebeeckx, K.H. Schmidt, O. Serot, S. Simakov, I. Sirakov, H. Sjöstrand, A. Stankovskiy, J.C. Sublet, P. Tamagno, A. Trkov, S. Van Der Marck, F. Álvarez-Velarde, R. Villari, T.C. Ware, K. Yokoyama, G. Žerovnik, The joint evaluated fission and fusion nuclear data library, JEFF-3.3, Eur. Phys. J. A 56 (2020) 181, http://dx.doi.org/10.1140/epja/s10050-020-00141-9.

[9] A. Davis, A. Turner, Comparison of global variance reduction techniques for Monte Carlo radiation transport simulations of ITER, Fusion Eng. Des. 86 (9–11) (2011) 2698–2700, http://dx.doi.org/10.1016/J.FUSENGDES.2011.01.059.

[10] J.-C. Sublet, L.W. Packer, J. Kopecky, R.A. Forrest, A.J. Koning, D.A. Rochman, The European Activation File: EAF-2010 Neutron-Induced Cross Section Library, Tech. rep. CCFE Report, CCFE–R (10) 05, 2010.

[11] J.C. Sublet, J.W. Eastwood, J.G. Morgan, M.R. Gilbert, M. Fleming, W. Arter, FISPACT-II: An advanced simulation system for activation, transmutation and material modelling, Nucl. Data Sheets 139 (2017) 77–137, http://dx.doi.org/10.1016/J.NDS.2017.01.002.

[12] H. Smith, ICRP Publication 74: Conversion Coefficients for use in Radiological Protection against External Radiation, Ann. ICRP 26 (3) (1996) 1–205, http://dx.doi.org/10.1177/ANIB_26_3-4.

[13] A. Čufar, A. Bruschi, U. Fischer, T. Franke, G. Granucci, G. Grossetti, I.A. Kodeli, D. Trombetta, R. Villari, Equatorial electron cyclotron port plug neutronic analyses for the EU DEMO, Fusion Eng. Des. 146 (2019) 336–340, http://dx.doi.org/10.1016/J.FUSENGDES.2018.12.062.

[14] A. Čufar, C. Bachmann, T. Berry, R. Chavan, T. Eade, T. Franke, B. Kos, D. Leichtle, P. Spaeh, M.Q. Tran, Neutronics analyses of EU DEMO 2020 EC port configuration (Poster presented at 30th International Conference NENE 2021, 6th–9th September 2021), 2021.